Biomimetic Cu, Zn and Cu2 complexes inserted in mesoporous silica as catalysts for superoxide dismutation

Matías Patriarca, Veronica Daier, Gerardo Camí, Nora Pellegri, Eric Rivière, Christelle Hureau, Sandra Signorella

Biomimetic Cu,Zn and Cu_2 complexes inserted in Mesoporous Silica as Catalysts for Superoxide Dismutation

Matías Patriarca,[a] Verónica Daier,[a,*] Gerardo Camí,[a] Nora Pellegri,[b] Eric Rivière,[c] Christelle Hureau,[d] and Sandra Signorella[a,*]

[a]*IQUIR (Instituto de Química Rosario), Consejo Nacional de Investigaciones Científicas y Técnicas (CONICET), Facultad de Ciencias Bioquímicas y Farmacéuticas, Universidad Nacional de Rosario, Suipacha 531, S2002LRK Rosario, Argentina*

[b]*Laboratorio de Materiales Cerámicos, FCEIyA, Universidad Nacional de Rosario, Av. Pellegrini 250, 2000 Rosario, Santa Fe, Argentina and IFIR, CONICET, 27 de Febrero 210 bis, 2000 Rosario, Santa Fe, Argentina*

[c]*Institut de Chimie Moléculaire et des Matériaux d'Orsay, CNRS, Université Paris Sud, Université Paris Saclay, 91405 Orsay Cedex, France*

[d]*LCC-CNRS, Université de Toulouse, 205 route de Narbonne, 31077 Toulouse, France*

*Corresponding authors:

E-mail: signorella@iquir-conicet.gov.ar; daier@iquir-conicet.gov.ar

Abstract

Three CuZn-superoxide dismutase (SOD) functional mimics, $[CuZn(dien)_2(\mu\text{-}Im)](ClO_4)_3$ (**1**), $[Cu_2(dien)_2(\mu\text{-}Im)](ClO_4)_3$ (**2**) (Im = imidazole, dien = diethylenetriamine), and $[CuZn(salpn)Cl_2]$ (**3**) (H_2salpn = 1,3-bis(salicylideneamino)propane), were successfully inserted into the nanochannels of SBA-15 type mesoporous silica with retention of the silica mesostructure. X-ray absorption spectroscopic studies indicate that the encapsulated complexes keep unchanged the first-shell environment of Cu(II) and Zn(II) ions. Magnetic measurements suggest that the nanochannels constrain the geometry of the μ-imidazolate-$Cu(II)_2$ core modifying the relative orientation of the two copper coordination planes. Confinement imposed by the silica nanochannels upon encapsulation of complexes **1** and **2** leads to stable hybrid materials at physiological pH with enhanced SOD activity relative to the free complexes. Unlike the imidazolato-bridged compounds, insertion of **3** in mesoporous silica leads to a less stable hybrid material exhibiting partial release into the aqueous solution and $O_2^{\bullet-}$ dismutation rate slower than the free complex. The covalent binding of a mononuclear $Cu(dien)Im^+$ moiety to the mesoporous silica showed lower SOD activity than encapsulated imidazolato-bridged CuZn and Cu_2 complexes. The results emphasize the positive effect of encapsulation on SOD activity of imidazolato-bridged dinuclear complexes.

Keywords

Hybrid materials; copper/zinc complexes; SOD mimics; mesoporous silica

1. INTRODUCTION

Pathological oxidative stress is caused by the imbalance between the production of reactive oxygen species (ROS) and the ability of a biological system to rapidly remove them or repair the resulting damage [1]. A particularly destructive aspect of oxidative stress is the production of free radicals and peroxides. The superoxide radical anion ($O_2^{\bullet -}$), a less reactive species formed by the one-electron reduction of O_2 during normal cellular metabolism, is the primary source of the deleterious hydroxyl radical ($HO^{\bullet}$) and hydrogen peroxide (H_2O_2) that can cause extensive cellular damage, and its overproduction is associated with a number of diseases, such as atherosclerosis, Parkinson's and Alzheimer's [2-4]. Superoxide dismutase enzymes (SODs) are a group of metalloenzymes which constitute the main biological defense against $O_2^{\bullet -}$ and are present in aerobic, aero-tolerant organisms and some obligate anaerobes [5]. These enzymes convert $O_2^{\bullet -}$ into O_2 and H_2O_2 at virtually diffusion controlled rates. Among them, CuZn-SOD is the most abundant and can be found in the chloroplast, in the cytosol and in the extracellular space [6]. Exogenous SOD enzymes have been tested as therapeutic agents to reduce oxidative stress damage with limited success mainly due to its large size, antigenicity and rapid elimination from the body [7,8]. Therefore, efforts have been focused on the design of low molecular-weight antioxidant catalysts (SOD-mimics) as potential therapeutic agents with better bioavailability than exogenously administered SOD enzymes [9]. A number of heterodinuclear CuZn and homodinuclear Cu_2 complexes have been evaluated as CuZn-SOD mimics [10-17]. For these complexes, k_{cat} values are one or two orders of magnitude higher than for $O_2^{\bullet -}$ self-disproportionation (k_{disp} = 5 x 10^5 M^{-1} s^{-1}, pH 7) [18]. In contrast to the enzyme, where the proteic framework protects the active site, a difficulty found in homogeneous systems is the poor stability of mimetic

complexes in solution, mainly due to hydrolysis, metal dissociation and formation of oligomers [10]. Because of its large surface area, controllable mesostructure, good mechanical and chemical stability and easily modifiable surface, mesostructured porous silica is a suitable matrix for encapsulating biomimetic complexes [19]. Insertion of the a biomimetic catalyst in this inorganic matrix can be used to reproduce certain properties of the native active site, such as confinement and site isolation, conferring stability to the complex while retaining, or even enhancing, its catalytic actvity [20-25].

With the aim to mimic the local cage effect around the active center of the enzyme, three CuZn-SOD functional mimics, $[CuZn(dien)_2(\mu\text{-}Im)](ClO_4)_3$ (**1**), $[Cu_2(dien)_2(\mu\text{-}Im)](ClO_4)_3$ (**2**) (Im = imidazole, dien = diethylenetriamine), and $[CuZn(salpn)Cl_2]$ (**3**) (H_2salpn = 1,3-bis(salicylideneamino)propane) [10], shown in Figure 1, were inserted into the nanochannels of mesoporous silica (SBA-15 type), and the resulting materials were characterized and evaluated as $O_2^{\bullet-}$ scavengers. Results obtained with encapsulated and free complexes were compared in order to highlight the role of nanochannels of mesoporous silica on SOD activity and catalyst stability. Additionally, the stability and SOD activity of encapsulated catalysts were compared to $[Cu(N_3pr)Im]^+$ (**2a**) (**N_3pr** = N-propyldiethylenetriamine) (Figure 1) covalently anchored to the mesoporous SBA-15 silica. The results presented here emphasize the positive effect of encapsulation on SOD activity of imidazolato-bridged dinuclear complexes that are structural mimics of the active site of CuZn-SOD.

2. EXPERIMENTAL

2.1. Synthesis of Complexes

$[CuZn(dien)_2(\mu\text{-Im})](ClO_4)_3$ (**1**), $[Cu_2(dien)_2(\mu\text{-Im})](ClO_4)_3$ (**2**), and $[CuZn(salpn)Cl_2]$ (**3**) were synthesized as previously described in reference 10. Anal. Calc. for $CuZnC_{11}Cl_3N_8H_{33}O_{14}$: C 17.9, Cu 8.6, H 4.5, N 15.2, Zn 8.9%; found: C 17.8, Cu 8.9, H 4.5, N 15.3, Zn 9.0%. Anal. Calc. for $Cu_2C_{11}Cl_3N_8H_{29}O_{12}$: C 18.9, H 4.2, N 16.0, Cu 18.5%; found: C 18.6, H 4.4, N 15.8, Cu 18.1%. Anal. Calc. for $CuZnC_{17}Cl_2H_{16}N_2O_2$: C 42.5, H 3.5, N 5.8, Cu 13.2, Zn 13.6%. Found: C 42.5, H 3.3, N 5.7, Cu 13.8, Zn 13.6%.

2.2. Synthesis of mesoporous SBA-15 silica

Pluronic P-123 (4.07 g) was dissolved in 30 mL distilled water and 120 mL 2 M hydrochloric acid in a Nalgene bottle at 35ºC. Then, 9 mL of tetraethoxysilane (TEOS) were added and the mixture was stirred (600 rpm) at 35ºC for 20 h. The resulting white suspension was then left at 85ºC for 24 h without stirring. After cooling to room temperature, the copolymer was removed by washing with distilled water and ethanol using a sintered disc filter funnel grade 4 [26]. The product was dried under vacuum at room temperature overnight and then calcined at 550ºC for 12 h.

2.3. Encapsulation of complexes 1 – 3 in mesoporous SBA-15 silica

Complexes **1** – **3** were immobilized following the same procedure. In a typical experiment, 0.3 g of SBA-15 were added to a solution of complex (0.20 mmol) in 20 mL of methanol. The mixture was stirred for 24 h at room temperature, filtered, and washed with methanol. The solid material was re-suspended in methanol and stirred overnight to remove residues. The solid was filtered and dried under vacuum until constant weight. Residual mass (%) at 700ºC: 88.2 (**1**@SBA-15); 95.0 (**2**@SBA-15); 84.7 (**3**@SBA-15). Cu wt %: 2.7 (**1**@SBA-15); 2.2 (**2**@SBA-15); 2.9 (**3**@SBA-15).

2.4. Obtention of 2a@SBA-15

N1-(3-Trimehoxysilylpropyl)diethylenetriamine (15.6 μL) was added to a suspension of 0.3 g of SBA-15 in 20 mL of ethanol and left at reflux with stirring during 6 h. Then, the suspension was centrifuged at 18000 rpm for 15 min, and the solid (**N_3pr**@SBA-15) was re-dispersed in ethanol and filtered several times using a sintered disc filter funnel grade 4, and finally dried under vacuum. Afterwards, 150 mg of **N_3pr**@SBA-15 were added to a solution containing $Cu(ClO_4)_2 \cdot 6H_2O$ (15.6 mg) and imidazole (3.8 mg) in 20 mL of methanol and left with stirring for 24 h. The solid, was filtered, washed several times with methanol and dried under vacuum overnight, to yield 152 mg of **2a**@SBA-15 (Scheme 1). Residual mass (%) at 700ºC: 86.6. Cu wt %: 2.55.

2.5. Physical measurements

UV-visible spectra were registered with a JASCO V-550 spectrophotometer. The spectra were collected in the range of 300 to 900 nm. EPR spectra of solid samples were obtained on an Elexsys E 500 Bruker spectrometer, operating at a microwave frequency of approximately 9.5 GHz, at 120 K. IR spectra were recorded on a Perkin-Elmer Spectrum One FT-IR spectrophotometer. Solid samples of silica, neat complexes and hybrid materials were run in ATR (attenuated total reflectance) mode on a diamond crystal. Principal components analysis (PCA) of IR spectral data was performed using the Statistica software [27], in the 1200 – 1800 cm^{-1} spectral region, selecting 313 wave numbers, with 34 principal components that justify 100% variance. Metal content was determinated by atomic absorption measurements on a Metrolab 250 AA spectrophotometer. Magnetic susceptibility data were collected with a Quantum Design MPMS SQUID susceptometer.

Thermogravimetric analyses (TGA) were carried out on a TGA 51 Shimadzu thermogravimetric analyzer and on a Perkin-Elmer Diamond TG/DTA Instrument. The heating rate was 10ºC min^{-1}, and the carrier gas (air) flow rate was 50 mL min^{-1}. Cu and Zn K-edge XANES (X-ray absorption near edge structure) spectra were recorded at the BM30B (FAME) beam line of the European Synchrotron Radiation Facility (ESRF, Grenoble, France) [28]. The beam energy was selected using an Si(220) N_2 cryo-cooled double-crystal monochromator with an experimental resolution close to that theoretically predicted (namely ~0.5 eV) [29]. The beam spot on the sample was approximately 300 × 200 μm^2 (H × V, FWHM). Spectra were recorded in absorption mode with a 30-element solid state Ge detector (Canberra) in liquid cells in a He cryostat. The temperature was kept at 10 K during data collection to prevent sample damage and the absence of significant photo-reduction of the Cu(II) samples was checked. The energy was calibrated with Cu and Zn metallic foils, such that the maximum of the first derivative was set at 8979 and 9659 eV, respectively. Cu data were collected from 8840 to 8960 eV using a 5 eV step of 2 s, from 8960 to 9020 eV using a 0.5 eV step of 3 s, and from 9020 to 9300 eV with a k-step of 0.05 $Å^{-1}$ and an increasing time of 2–10 s per step. Zn data were collected from 9510 to 9630 eV using a 5 eV step of 2 s, from 9630 to 9700 eV using a 0.5 eV step of 3 s, and from 9700 to 10,000 eV with a k-step of 0.05 $Å^{-1}$ and an increasing time of 2–10 s per step. XANES spectra were background-corrected by a linear regression through the pre-edge region and a polynomial through the post-edge region and normalized to the edge jump. XANES of the neat samples were prepared in a BN matrix (diluted to approximately 5%). Porosity and surface area were determined from N_2 adsorption-desorption isotherms obtained at 77 K on a Micrometric ASAP 2020 V4.02 (V4.02 G) apparatus. The samples were degassed at 10^{-3} Torr and 200 ºC for 6 h prior to the

adsorption experiment. Surface area (S_{BET}) were calculated using the Brunauer-Emmett-Teller (BET) [30] equation over the pressure range (p/p^o) of 0.05-0.20. The volume of micropores and mesopores ($V_{\mu P}$ and V_{MP}) was determined by the alpha-plot method [30] using the standard Licrospher isotherm. The total pore volume (V_{TP}) was determined with the Gurvich rule [30] at 0.98 p/p^o. The pore size distributions were calculated using the Villarroel–Bezerra–Sapag (VBS) model [31], on the desorption branch of the N_2 isotherms. The VBS method adds a correction term to the original Kelvin equation, providing more accurate values for the pore size. The size and morphology of solid materials were recorded using a FEI Quanta 200 FEG scanning electron microscope (SEM) operated at variable accelerating voltages and with EDS detector. The samples were prepared by dispersion of the mesoporous dry silica and hybrid samples over a carbon film. Transmission electron microscopy (TEM) analysis was performed with a S/TEM JEM 2100 Plus with operational voltage of 200kV (variable), with a LaB6 filament. The samples were prepared dispersing the material in ethanol and depositing it on Formvar/Carbon square mesh Cu, 400 Mesh grids.

2.6. Indirect SOD assay

The SOD activity of the free and immobilized complexes was evaluated by measuring the inhibition of the photoreduction of nitro blue tetrazolium (NBT), by a method slightly modified from the originally described by Beauchamps and Fridovich [32]. Reaction of methionine and riboflavin, in the presence of light, is the source of superoxide. The suspensions were prepared in 50 mM phosphate buffer of pH 7.8, riboflavin (3.4 μM), methionine (10 mM), NBT (46 μM) and different amounts of adsorbed complexes (0-100 μM). Riboflavin was last added and the reaction was

initiated by illumination of the mixtures with a 18 W fluorescent lamp placed at 15 cm, at 25ºC [33]. The reduction of NBT was measured at 560 nm after an illumination period of 15 min. The IC_{50} values (the concentration of the SOD mimic that induces a 50% inhibition of the reduction of NBT) were determined from concentration-dependent plots. Control reactions confirm that the compounds did not react directly with NBT or riboflavin. Inhibition percentage was calculated according to:

$\{(\Delta Abs/t)_{without\ catalyst} - (\Delta Abs/t)_{with\ catalyst}\} \times 100 / (\Delta Abs/t)_{without\ catalyst}$.

3. RESULTS and DISCUSSION

3.1. Morphology of the mesoporous silica and hybrid materials

Well-ordered mesoporous SBA-15 silica particles were synthesized using the triblock copolymer Pluronic P-123 as structure directing agent, in strong acid media and heating the reaction mixture at 85ºC for 24 h. The TEM images of the calcined sample of mesoporous silica (Figure 2(a)) show a regular array of cylindrical channels along the long axis of the particles, thereby confirming that the calcined silica has a highly ordered mesostructure, with estimated pore diameter of ~ 5-10 nm (in agreement with N_2 sorption results, discussed in section 3.2). It can also be observed that the channel openings are fully exposed at the surface of the individual particles (Figure S1(a)), and therefore, are suitable for the insertion of complexes which are ~ 1.25-1.27 nm wide (calculated from crystal structures [10,34]). SEM images of SBA-15 silica show independent oblong (length:width ratio = 2.2:1) particles linearly grouped forming long chain structures of 20-40 μm length (Figure 2(b,c)). Image-J analysis gave particle size distribution in the range of 727 ± 234 nm. Taking advantage of the high affinity of positively charged species for SBA-15 silica, insertion of the cationic complexes **1**, **2** and **3** into the mesoporous SBA-15 silica was

performed by ionic exchange (exchange of silanol protons by the cationic complexes that bind the negatively charged Si-O^- groups of the SBA-15 surface), as shown in eq. (1).

$$n\ \text{-SiOH} + \text{catalyst}^{n+} \rightleftharpoons (\text{-SiO})_n\text{Catalyst} + n\ H^+ \qquad (1)$$

Compared to the parent SBA-15, the particle size of the hybrid materials decreased and the chain array was not retained, as shown in Figure 2(d) for **2**@SBA-15, and S1(b,c) for **1**@SBA-15 and **3**@SBA-15. In the case of mesoporous silica covalently functionalized with triamine group, **N_3pr**@SBA-15, SEM images show entangled assemblies of oblong particles of ~ 1 μm length (Figure 2(e)). Binding of the $Cu(Im)^+$ moiety to the triamine groups of silica resulted in particles of **2a**@SBA-15 < 1 μm with similar shape and arrangement as **N_3pr**@SBA-15 (Figure 2(f)).

3.2. Textural characterization

Nitrogen adsorption-desorption isotherms at 77K for unmodified SBA-15 and hybrid materials are given in Figure 3, while pore size distributions are shown in Figure S2. All the samples exhibit a typical type IV isotherm with H1 hysteresis loop at high relative pressure (p/p^0 = 0.6–0.8), which is characteristic of ordered mesoporous materials [35]. The p/p^0 positions of the inflection points are related to the diameter in the mesopore range, and the sharpness of the step indicates the uniformity of the mesopore size distribution. The results indicate that the mesoporous structure of SBA-15 silica has been successfully retained in the modified materials. However, there is a shift of the hysteresis position towards lower p/p^0 values along with a decrease in overall nitrogen adsorption volume with increasing surface coverage. The textural data of all the mesoporous materials are summarized in Table 1. The BET surface area, pore volume and average pore diameter of the hybrid materials

decrease compared to pure SBA-15 silica, which is consistent with the presence of complexes inside the channels of SBA-15.

The pore diameter distribution in the modified silicas indicates that the mesopore uniformity of the parent SBA-15 is retained. In all cases, secondary mesoporosity (disordered mesopores) and particles agglomerates were evidenced and taken into account for calculation of textural parameters.

3.3. Chemical characterization of the hybrid materials

3.3.1. IR spectroscopy

FT-IR spectra of hybrid materials provided surface information useful for the identification of some of the functional groups present in the immobilized complexes (Figure S3). In the IR spectra of SBA-15 and hybrid materials the Si-O-Si framework can be easily identified by the bands at 1080 cm^{-1} (ν_{as}, Si-O), 795 cm^{-1} (ν_{s}, Si-O) and 463 cm^{-1} (δ, Si-O-Si) [36]. Spectra of **1**@SBA-15 and **2**@SBA-15 show absorption bands at 1585 and 1460 cm^{-1} characteristic of vibration of the imidazolate ring skeleton, the stretching bands of saturated C-H and unsaturated C-H at 2935 $cm^{-1}$and 3150 cm^{-1}, respectively, and N-H stretching at 3280, 3240 cm^{-1}, confirming that the two complexes were successfully encapsulated in the framework of mesoporous SBA-15 silica. The spectrum of **3**@SBA-15 displays bands at 1616, 1600, 1560 and 1480 cm^{-1}, which can be assigned to the salpn ligand, suggesting this complex has also been inserted in the SBA-15 silica matrix by ion exchange. The assignment of the IR bands of the complexes immobilized in the mesoporous silica was verified and confirmed by principal component analysis (PCA) of the spectra in the 1200 – 1800 cm^{-1} spectral range [37,38], from multiple spectra taken on silica, neat complexes and hybrid materials.

3.3.2. Thermogravimetric analysis (TGA)

Thermogravimetric profiles of hybrid materials measured under air (Figure S4) showed a first weight loss below 200ºC due to removal of physically adsorbed water molecules, and a second weight loss from 250 to 350ºC for **1**@SBA-15 and **2**@SBA-15, around 355ºC for **3**@SBA-15 and from 220 to 600ºC for **2a**@SBA-15, assigned to decomposition of the organic ligands. The second mass loss corresponds to 14% (**1**@SBA-15), 4.6% (**2**@SBA-15), 13% (**3**@SBA-15), and 8.6% (**2a**@SBA-15). Complexes **1** and **2** decompose at 250ºC and complex **3** at 310ºC. Therefore, the temperature required for total weight loss of immobilized complexes is higher than for the free compounds, indicating that the mesoporous silica protects them against heat decomposition. Weight loss data together with the results of metal analyses were employed to calculate the amount of complex present in the hybrid materials, listed in Table 2. The lower proportion of **2** encapsulated into mesoporous silica agrees with the smaller decrease in the pore volume and surface area (Table 1) measured for this complex.

3.3.3. Cu and Zn K-edge XANES

X-ray Absorption Near-Edge Structure (XANES) spectroscopic analysis was performed on the free and encapsulated complexes to compare the first-shell environment of the metal centers. Indeed Cu and Zn K-edge absorptions are sensitive to the metal center environment. The Cu K-edge XANES spectra of all the three complexes and hybrid materials show characteristic features of square-planar coordinated Cu(II) ion (Figure 4, left) [39-42]. Cu K-edge spectra of the neat complexes and their corresponding hybrid materials are virtually superimposable,

indicating that the first-coordination sphere of Cu(II) is maintained upon the insertion in SBA-15. It is also worth noting that **1** and **2** show very similar XANES fingerprints in line with a weak effect of Cu(II) or Zn(II) being the second metal center of the dinuclear species and with a similar environment of the two Cu(II) centers in **2**.

The Zn K-edge XANES spectra (Figure 4, right) show a steeply rising edge structure with a maximal normalized absorption intensity of about 1.4 typical of Zn(II) in a distorted tetrahedral geometry [43]. Spectra of complex **3** and its hybrid material are almost superimposable and confirm that only limited structural differences exist between the Zn(II) sites in the free and encapsulated complexes. For complex **1**, there is a small difference tentatively attributed to the presence of a slight amount of ligand-unbound Zn(II) ion (i.e. hexa-aquo) in the neat powder which is not inserted into the material [44].

3.3.4. EPR Spectroscopy and magnetization measurements

Low temperature X-band EPR spectra of complexes inserted in the mesoporous silica provided details on the geometry and coordination environment of Cu(II) ions in the hybrid materials. A powdered sample of complex **1** exhibits the usual line shape for mononuclear Cu(II) sites with $g_{//} > g_{\perp} > 2.03$, indicating an axial symmetry (Figure 5(a), top), with $g_{\perp} = 2.05$ and $g_{//} = 2.20$. In the **1**@SBA-15 hybrid, *g*-factors are retained (Table S1), suggesting no significant change of the coordination geometry of Cu(II) in the hybrid. As a consequence of the dilution of the complex in the diamagnetic silica matrix, hyperfine splitting in the parallel region could resolve (Figure 5(a), bottom), with $A_{//} = 184 \times 10^{-4}$ cm^{-1} and $g_{//}/A_{//}$ ratio (*f*-factor) of 120 cm denoting a slightly distorted N_4-square planar geometry with a d_{x2-y2} ground state. The *f*-factor of **1**@SBA-15 is slightly larger than for a frozen solution of **1** in DMSO

(114 cm) [10], indicating a somewhat greater distortion of the complex within the SBA-15 matrix. Complex **2** contains two Cu(II) centers separated by ~ 5.8 Å [34]. For a coupled $Cu(II)_2$ system, $\Delta M_S = \pm 1$ transitions within the triplet state are expected on either side of $g = 2$ with the overall width of the resonance determined by the Cu···Cu distance [45,46]. No resonances below 2800 and above 3400 G and no half-field transition $\Delta M_S = \pm 2$, attributable to a magnetic coupling between two Cu(II) ions, were detected for **2** (Figure 5(b), top). Besides, the EPR signal of the neat complex is broadened due to dipolar and spin-spin intermolecular interactions so that structural information from hyperfine coupling between the unpaired electron and copper ions is lost. Encapsulation of the complex in the mesoporous silica results in dilution of the paramagnetic centers in the diamagnetic matrix yielding a better defined axial EPR signal with spectral parameters $g_\perp = 2.07$ and $g_{//} = 2.16$ characteristic of tetragonal Cu(II) ions with a d_{x2-y2} ground state (Figure 5(b), middle). The lack of transitions belonging to the triplet state might arise from the constrained geometry of the μ-imidazolate-$Cu(II)_2$ core in the channels of SBA-15 silica. Hyperfine features due to Cu(II) could be resolved in the parallel region for the covalently bound mononuclear Cu(II) complex, **2a**@SBA-15, which exhibits a spectrum typical of Cu(II) in tetragonal geometry (Figure 5(b), bottom), with spectral parameters $g_\perp = 2.04$, $g_{//} = 2.24$ and well resolved $A_{//} = 186 \times 10^{-4}$ cm^{-1} (Table S1). Here again, the tetrahedral distortion from square planar geometry in **2a**@SBA-15 (*f*-factor = 120 cm) is slightly larger than for the free complex in frozen DMSO solution (*f*-factor = 115 cm [47]).

The EPR spectrum of **3** (Figure 5(c), top) evidences the formation of dimeric species with the main signal at g_1 flanked by the $\Delta M_S = \pm 1$ transitions from the triplet state of a spin-coupled $Cu(II)_2$ system (g_2, g_3). Interestingly, the spectrum of **3**@SBA-15

(Figure 5(c), middle) shows that encapsulation drives out intermolecular interactions between individual paramagnetic centers, and thereby the axial spectrum of individual complexes can be observed, with spectral parameters $g_{\perp}$ = 2.04, $g_{//}$ = 2.24. EPR signals of the hybrid are still broad probably due to the overlap of species with slightly different geometries in the silica channels. For comparison, the spectrum of powdered neat **Cu(salpn)**, with typical axial *g*-factor components is shown in Figure 5(c), bottom.

Variable-temperature magnetic susceptibility (χ_M) measurements on hybrid materials confirm the EPR results. Plots of the $\chi_M T$ *vs T*, and low temperature magnetic isotherms are shown in figure S5. For **1**@SBA-15, $\chi_M T$ at room temperature (0.39 $cm^3\ mol^{-1}\ K$) is close to the expected value for a magnetically uncoupled spin S = 1/2 system and remains constant over the full range of temperature. **3**@SBA-15 shows the same behavior from 300 K to 10 K and then decreases down to 0.29 $cm^3\ mol^{-1}\ K$ at 2 K, indicating weak intermolecular magnetic interactions. In Figure S5(a,c), the magnetic isotherms of **1**@SBA-15 and **3**@SBA-15 are compared to the free complexes. It can be observed that while magnetization curves for **1** and **1**@SBA-15 overlap, for **3** and **3**@SBA-15 curves are not superimposed as a consequence of the larger intermolecular interactions in the neat complex. For **2**@SBA-15, $\chi_M T$ at room temperature (0.8 $cm^3\ mol^{-1}\ K$) is slightly above the expected value for two magnetically uncoupled Cu(II) centers. When lowering the temperature, the $\chi_M T$ value remains approximately constant down to ca. 15 K and then decreases reaching a value of 0.77 at 2 K (Figure S5(b)). This behavior suggests a feeble antiferromagnetic interaction between the two Cu(II) ions in **2**@SBA-15, much weaker than observed for the neat sample (Figure 5S(b), J = -68.9 cm^{-1} [10]). Constraints imposed by the silica matrix should modify the relative orientation of the

two metal centers of the μ-imidazolate-Cu(II)$_2$ core affording an extremely weakly coupled system, in agreement with EPR results.

3.4. Stability of complexes immobilized in SBA-15

Given the free complex and Cu^{2+}_{aq} catalyze $O_2^{\bullet -}$ dismutation, reliable SOD measurements require controlling the possible complex or metal leaching into the solvent. To check the stability of the immobilized complexes, the hybrids materials were incubated in phosphate buffer of pH 7.8 for different times, and UV-Vis spectra were registered on the supernatant after centrifugation of the suspensions. The incubation time was at least 15 min, the time-length of the SOD's test.

In Figure 6 spectra taken after different incubation times are compared to the electronic spectra of the free complex solutions. Absorbance' increase observed for the encapsulated complexes **1**@SBA-15 and **2**@SBA-15 was less than 1% after 1 day, therefore the SOD activity, if any, must be due to the complex inserted into the silica channels. For **3**@SBA-15, the absorbance increases 9% after 15 min of incubation, so this contribution must be taken into account when evaluating the SOD activity of this material. In the case of the covalently bound complex **2a**@SBA-15, absorbance increases 17% after 15 min probably due to $CuIm^+$ leached from the silica surface (in this material, the complex is anchored inside the channels but also on the surface of the silica). Therefore, covalent binding leads to a less stable hybrid material at physiological pH.

3.5. SOD-like Activity

The general reaction for the catalyzed $O_2^{\bullet -}$ disproportionation is shown in eqs. 2-3.

$$Catalyst_{ox}^{n+} + O_2^{\bullet-} \rightarrow Catalyst_{red}^{(n-1)+} + O_2 \quad (2)$$

$$Catalyst_{red}^{(n-1)+} + O_2^{\bullet-} (2H^+) \rightarrow Catalyst_{ox}^{n+} + H_2O_2 \quad (3)$$

The SOD activity of adsorbed complexes was measured by the Beauchamps and Fridovich assay using the NBT reagent, at pH 7.8 [32]. This assay is based on kinetic competition between NBT and the catalyst for reaction with superoxide. In this way, the SOD activity is inversely related to the amount of formazan, the purple product formed by reaction of NBT with superoxide, observed at 560 nm. The four hybrid materials exhibit activity towards dismutation of superoxide, as shown in Figure 7. The graphically evaluated IC_{50} values (amount of catalyst required for 50% inhibition of superoxide reduction) and calculated rate constants (k_{McF}) are listed in Table 3. The k_{McF} are calculated at 50% inhibition, where the rates of reactions of NBT and adsorbed complex are equal, k_{McF} [catalyst] = k_{NBT} [NBT], and therefore $k_{McF} = k_{NBT}$ [NBT]/IC_{50}. [48]. These values are independent of the detector concentration and appropriate for comparison with literature values.

The relative values of k_{McF} calculated for free and immobilized complexes **1** and **2** demonstrate that encapsulation of these complexes in the mesoporous silica enhances 3- to 4-times their SOD activity (Table 3). Confinement imposed by the silica nanochannels results in local distortion of the Cu center larger than in the free complexes (as discussed above) and can account for this difference. It has been observed that a distorted square-planar geometry, close to the geometry of native SOD (*f*-factor = 160 cm [49]), favors catalytic activity [24]. Another important effect of pore confinement is to keep the Cu active site and imidazolate group in close proximity to regenerate the complex during the catalytic cycle, such as shown in Scheme 2. The superoxide dismutation catalyzed by these SOD-mimics involves

reduction of Cu(II) by one $O_2^{\bullet-}$ to form O_2, and re-oxidation of Cu(I) by a second $O_2^{\bullet-}$ to form H_2O_2 [5]. While in the cupric form of the catalyst, copper is tetracoordinated to dien and imidazolate, in the cuprous form, the copper-imidazolate bond breaks, Cu(I) becomes three-coordinate bound to dien only and protonated imidazole is left binding exclusively to the Zn ion, which remains tetrahedral. Therefore, constrained by the nanochannel size, the imidazole-Zn moiety remains close to the copper center facilitating the re-binding of imidazolate to the oxidized Cu(II) improving the efficiency of the catalytic cycle. In line with this, encapsulation of another imidazolato-bridged CuZn complex, $[(dien)Cu(\mu\text{-}Im)Zn(tren)]^{3+}$ (tren = tris(2-aminoethyl)amine) (**5**, Table 3) in mesoporous silicas had been reported to improve the SOD activity of the complex [24], although in a lesser extent than observed for **1** and **2**. These authors observed the best SOD activity when complex **5** was inserted into aluminosilicate functionalized with alkylamonium groups (k_{McF} = 1.5 x 10^8 M^{-1} s^{-1}).

The covalent binding of a mononuclear Cu(II) center to the mesoporous silica showed lower SOD activity than imidazolato-bridged CuZn and Cu_2 complexes encapsulated by ionic exchange (Table 3), probably due to the proportion of the complex grafted on the external surface of the mesoporous silica that can leach easier into the solution, and the lack of the second metal bound though imidazolate which avoids the ImH^+ moves away from the catalytic center, just as proposed for the enzyme [5,6].

Unlike imidazolato-bridged complexes, encapsulation of CuZn-salpn retards the $O_2^{\bullet-}$ dismutation rate that is even slower than for the free complex (Table 3). The low activity of this complex can be related to the low flexibility of the N_2O_2-ligand to accommodate Cu(I) and the partial release of complex into the bulk solution (as described in section 3.4).

CONCLUSIONS

Insertion of complexes **1**, **2** and **3** into mesoporous silica, by ionic exchange, leads to hybrid materials where the cationic complexes are encapsulated inside the silica nanochannels. Spectroscopic measurements confirmed the retention of the integrity of the dinuclear complexes and geometry around the metal ions: tetragonal for Cu(II) and tetrahedral for Zn(II), while magnetic measurements demonstrated that constraints imposed by the silica matrix modify the relative orientation of the coordination planes of the two metal centers of the imidazolato-bridged dicopper moiety affording a material where the two metal centers are very weakly coupled. Insertion of complexes **1** and **2** inside the mesoporous silica enhances their efficiency to catalyze $O_2^{\bullet-}$ disproportionation, probably because the confinement keeps the Cu(II) site and imidazolate group in close proximity to facilitate re-binding of imidazolate to the Cu(II) center during the catalytic cycle (as shown in Scheme 2). Unlike compounds **1** and **2**, encapsulation of **3** retards $O_2^{\bullet-}$ disproportionation rate. In this case, the nanochannel probably restrains the ligand rearrangement during the reaction to yield a tetragonal or trigonal-planar geometry around Cu(I). **1**@SBA-15 and **2**@SBA-15 hybrids are catalysts better than the covalently anchored mononuclear **2a**@SBA-15, which is partially bound to the silica external surface and easily released into the bulk solution. Based on these results, insertion of the catalyst into mesoporous silica by ionic exchange is a promising strategy for the design of therapeutic $O_2^{\bullet-}$ scavengers based on imidazolato-bridged CuZn or diCu complexes which are structural and functional mimics of the active site of the native enzyme. However, this approach cannot be generalized to any class of complexes, as exemplified by **3**.

ACKNOWLEDGMENTS

This work was supported by the National University of Rosario and the Consejo Nacional de Investigaciones Científicas y Técnicas (CONICET, PIP 0337), the Centre National de la Recherche Scientifique (CNRS, PICS 07121), and CONICET/CNRS bilateral agreement (Res. 991/13) and the Agency for Science, Technology and Innovation of Santa Fe (ASACTeI, IO 2010-164-16). We acknowledge ESRF for provision of synchrotron radiation on the FAME beamline (Proposal 30-02-1078 and 30-02-1126), the FAME team, and Dr. Laurent Sabater for his participation in data recording. M. Patriarca thanks Dr. Sapag for fruitful discussions on application of the VBS method.

Apendix A- Supplementary data

Supplementary data associated with this article can be found, in the online version, at https://doi.org/10.1016/j.micromeso.xxxx.

REFERENCES

[1] L. M. Sayre, G. Perry, M. A. Smith, Chem. Res. Toxicol. 21 (2008) 172−188.

[2] S. G. Rhee, T.-S. Chang, W. Jeong, D. Kang, Mol. Cells 29 (2010) 539–549.

[3] J. P. Kehrer, Toxicology 149 (2000) 43–50.

[4] C. Cheignon, M. Tomas, D. Bonnefont-Rousselot, P. Faller, C. Hureau, F. Collin, Redox Biology 14 (2018) 450-464

[5] Y. Sheng, I. A. Abreu, D. E. Cabelli, M. J. Maroney, A.-F. Miller, M. Teixeira, J. S. Valentine, Chem. Rev. 114 (2014) 3854–3918.

[6] I. A. Abreu, D. E. Cabelli, Biochim. Biophys. Acta 1804 (2010) 263–274.

[7] S. Cuzzocrea, D. P. Riley, A. P. Caputi, D. Salvemini, Pharmacol. Rev. 53 (2001) 135–159.

[8] D. P. Riley, Chem. Rev. 99 (1999) 2573–2588.

[9] S. Signorella, C. Palopoli, G. Ledesma, Coord. Chem. Rev. 365 (2018) 75-102.

[10] V. A. Daier, E. Rivière, S. Mallet-Ladeira, D. Moreno, C. Hureau, S. R. Signorella, J. Inorg. Biochem. 163 (2016) 162-175.

[11] C. Wang, S. Li, D.-J. Shang, X.-L. Wang, Z.-L. You, H.-B. Li, Bioorg. Med. Chem. Lett. 21 (2011) 4320–4324.

[12] Z.-P. Qi, K. Cai, Q. Yuan, T.-A. Okamura, Z.-S. Bai,W.-Y. Sun, N. Ueyama, Inorg. Chem. Commun. 13 (2010) 847–851.

[13] J. Han, Y. Xing, C. Wang, P. Hou, F. Bai, X. Zeng, X. Zhang, M. Ge, J. Coord. Chem. 62 (2009) 745–756.

[14] Q. Yuan, K. Cai, Z.-P. Qi, Z.-S. Bai, Z. Su, W.-Y. Sun, J. Inorg. Biochem. 103 (2009) 1156–1161.

[15] R.N. Patel, V.L.N. Gundla, D.K. Patel, Polyhedron 27 (2008) 1054–1060.

[16] H. Fu, Y.-H. Zhou, W.-L. Chen, Z.-G. Degin, M.-L. Tong, L.-N. Ji, Z.-W. Mao, J. Am. Chem. Soc. 128 (2006) 4924–4925.

[17] D. Li, S. Li, D. Yang, J. Yu, J. Huang, Y. Li, W. Tang, Inorg. Chem. 42 (2003) 6071–6080.

[18] B. H. Bielski, D. E. Cabelli, R. L. Arudi, A. B. Ross, J. Phys. Chem. Ref. Data 14 (1985) 1041–1106.

[19] B. Albela, L. Bonneviot, New J. Chem. 40 (2016) 4115-4131.

[20] K. Zhang, H.-L. Chen, B. Albela, J.-G. Jiang, Y.-M. Wang, M.-Y. He, L. Bonneviot, Eur. J. Inorg. Chem. (2011) 59-67.

[21] J. Chaignon, S.-E. Stiriba, F. Lloret, C.; Yuste, G. Pilet, L. Bonneviot, B. Albela, I. Castro, Dalton Trans. 43 (2014) 9704-9713.

[22] B. Garcia-Cirera, M. Corbella, L. Bonneviot, B. Albela, Micropor. Mesopor. Mater. 261 (2018) 150-157.

[23] L. Escriche-Tur, M. Corbella, M. Font-Bardia, I. Castro, L. Bonneviot and B. Albela, Inorg. Chem. 54 (2015) 10111-10125.

[24] Y. C. Fang, H. C. Lin, I. J. Hsu, T. S. Lin, C. Y. Mou, J. Phys. Chem. C 115 (2011) 20639–20652.

[25] I. Szilágyi, I. Labádi, K. Hernadi, I. Pálinkó, I. Fekete, L. Korecz, A. Rockenbauer, T. Kiss, New J. Chem. 29 (2005) 740 –745.

[26] J. P. Thielemann, F. Girgsdies, R. Schlögl, C. Hess, Beilstein J. Nanotechnol. 2 (2011) 110-118.

[27] Statistica - Data analysis software system, version 11, StatSoft, INC., 2012.

[28] O. Proux, X. Biquard, E. Lahera, J. J. Menthonnex, A. Prat, O. Ulrich, Y. Soldo, P. Trévisson, G. Kapoujvan, G. Perroux, P. Taunier, D. Grand, P. Jeantet, M. Deleglise, J.-P. Roux, J.-L. Hazemann, Phys. Scr. 115 (2005) 970–973.

[29] O. Proux, V. Nassif, A. Prat, O. Ulrich, E. Lahera, X. Biquard, J. J. Menthonnex, J.-L. Hazemann, J. Synchrotron Radiat. 13 (2006) 59–68.

[30] M. Thommes, K. Kaneko, A. V. Neimark, J. P. Olivier, F. Rodriguez-Reinoso, J. Rouquerol, K. S. W. Sing, Pure Appl. Chem. 87 (2015) 1051–1069.

[31] J. Villarroel Rocha, D. Barrera, K. Sapag, Top Catal. 54 (2011) 121–134.

[32] C. Beauchamps, I. Fridovich, Anal. Biochem. 44 (1971) 276–287.

[33] V. Daier, D. Moreno, C. Duhayon, J.-P. Tuchagues, S. Signorella, Eur. J. Inorg. Chem. (2010) 965–974.

[34] R. N. Patel, N. Singh, K. K. Shukla, U. K. Chauhan, CCDC 203653: Experimental Crystal Structure Determination, 2005

[35] K. S. W. Sing, Pure Appl. Chem. 57 (1985) 603–619.

[36] J. Cuan, B. Yan, Dalton Trans. 42 (2013) 14230–14239.

[37] I. T. Jolliffe, Principal Component Analysis, 2nd ed. Springer, 2002, p 487.

[38] R. A. Johnson, D. W. Wichern, Applied Multivariate Statistical Analysis, sixth ed. Pearson Education Limited, 2008, p 761.

[39] L. S. Kau, D. J. Spira-Solomon, J. E. Penner-Hahn, K. O. Hodgson, E. I. Solomon, J. Am. Chem. Soc. 109 (1987) 6433–6442.

[40] M. Sano, S. Komorita and H. Yamatera, Inorg. Chem. 31 (1992) 459-463.

[41] S. Della Longa, I. Ascone, A. Bianconi, A. Bonfigli, A. Congiu Castellano, A. Zarivi, M. miranda, J. Biol. Chem. 271 (1996) 21025-21030.

[42] E. Borghi, P. I. Solari, M. Beltramini, L. Bubacco, P. Di Muro, B. Salvato, Biophys J. 82 (2002) 3254-3298.

[43] L. Giachini, G. Veronesi, F. Francia, G. Venturolid, F. Boscherinib, J. Synchrotron Radiat. 17 (2010) 41– 52.

[44] J. Osán, F. Meirer, V. Groma, S. Török, D. Ingerle, C. Streli, G. Pepponi, Spectrochim. Acta Part B: At. Spectrosc. 65 (2010) 1008-1013.

[45] T. D. Smith, J. R. Pilbrow, Coord. Chem. Rev. 13 (1974) 173–278.

[46] K. Das, U. Panda, A. Datta, S. Roy, S. Mondal, C. Massera, T. Askun, P. Celikboyun, E. Garribba, C. Sinha, K. Anand, T. Akitsu, K. Kobayashi, New J. Chem. 39 (2015) 7309-7321.

[47] R. N. Patel, N. Singh, K. K. Shukla, U. K. Chauhan, Spectrochim. Acta A 61 (2005) 287–297.

[48] S. Durot, C. Policar, F. Cisnetti, F. Lambert, J. Renault, G. Pelosi, G. Blain, H. Korri-Youssoufi, J. Mahy, Eur. J. Inorg. Chem. (2005) 3513–3523.

[49] K. M. Beem, W. E. Rich, K. V. Rajagopa, J. Biol. Chem. 249 (1974) 7298–7305.

[50] G. Rotilio, R. C. Bray, E. M. Fielden, Biochim. Biophys. Acta 268 (1972) 605-609.

[51] Z. R. Liao, X. F. Zheng, B. S. Luo, L. R. Shen, D. F. Li, H. L. Liu, W. Zhao, Polyhedron 20 (2001) 2813–2821.

Table 1. Textural properties of materials

	S_{BET} [$m^2\ g^{-1}$]	V_{uP} [$cm^3\ g^{-1}$]	V_{MP} [$cm^3\ g^{-1}$]	V_{TP}[a] [$cm^3\ g^{-1}$]	W_p [nm]
SBA-15	450	0.01	0.48	0.71	8.6
1@SBA-15	210	0.01	0.13	0.37	7.5
2@SBA-15	380	0.01	0.40	0.68	8.4
3@SBA-15	250	0.01	0.17	0.41	6.9
N_3pr@SBA-15	621	0.05	0.52	0.68	6.3
2a@SBA-15	307	0.01	0.35	0.42	4.8

[a] $V_{TP} = V_{\mu P} + V_{primary\ MP} + V_{secondary\ MP}$, MP = mesopore; μP = micropore

Table 2. Amount of complex in the hybrid materials

	Sample			
	1@ SBA-15	**2**@SBA-15	**3**@SBA-15	**2a**@SBA15
mmol of complex/100 g of hybrid material	42	17	47	40

Table 3. SOD activity of free and immobilized complexes

Catalyst	IC_{50} [μM]	k_{McF} [M^{-1} s^{-1}][a]
1@SBA-15	0.109	25.1 x 10^6
2@SBA-15	0.116	23.5 x 10^6
2a@SBA-15	2.02	1.35 x 10^6
3@SBA-15	5.99	0.456 x 10^6
1	0.423	6.46 x 10^6 [10]
2	0.35	7.80 x 10^6 [10]
3	3.2	0.85 x 10^6 [10]
5@SBA-15		6.32 x 10^6 [24]
5@MCM-41		8.25 x 10^6 [24]
5		5.12 x 10^6 [24]
CuZn-SOD (native)		1800 x 10^6 [50]

[a]Calculated using k_{NBT} (pH = 7.8) = 5.94 x 10^4 M^{-1} s^{-1} [51].

5 = [(dien)Cu(μ-Im)Zn(tren)]$^{3+}$, tren = tris(2-aminoethyl)amine

Figures Captions

Figure 1. Complexes studied in this work. H are omitted for clarity

Figure 2. TEM image of SBA-15 (a) and SEM images of SBA-15 (b,c), **2**@SBA-15 (d), **N_3pr**@SBA-15 (e) and **2a**@SBA-15 (f).

Figure 3. N_2 Adsorption-Desorption Isotherms of materials at 77 K

Figure 4. XANES spectra of free and encapsulated complexes. Left: Cu K-edge. Right: Zn K-edge

Figure 5. X-band EPR spectra of solid samples of complexes and hybrid materials at 120 K

Figure 6. Electronic spectra of supernatant of hybrid suspensions after several incubation times in phosphate buffer of pH 7.8. (a) 1.1 mg/mL **1**@SBA-15, [**1**] = 0.44 mM; (b) 1.3 mg/mL **2**@SBA-15, [**2**] = 0.23 mM; (c) 0.65 mg/mL **3**@SBA-15, [**3**] = 0.14 mM; (d) 0.6 mg/mL **2a**@SBA-15, [**2**] = 0.23 mM

Figure 7: SOD activity of hybrids in the riboflavin-methionine-NBT assay

Schemes Captions

Scheme 1. Covalent binding of catalyst to mesoporous silica

Scheme 2. Disproportionation of $O_2^{\bullet-}$ by **1**@SBA-15

Figure 1

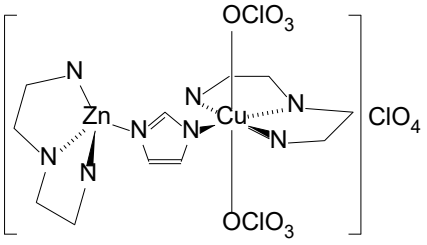

1

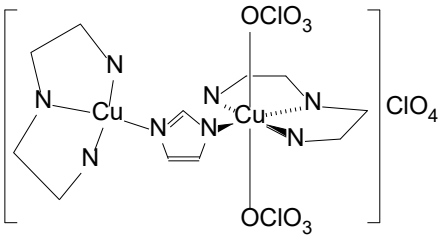

2

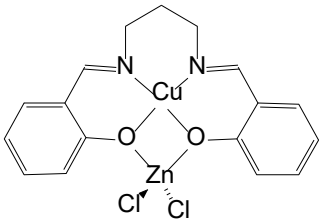

3

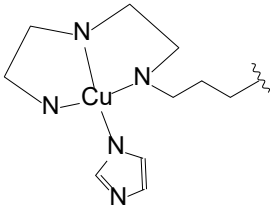

2a

Figure 2

(a)

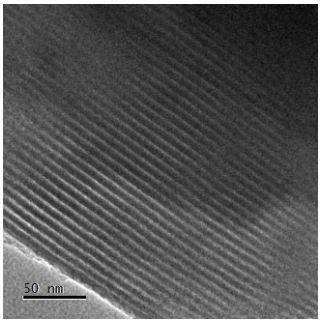

(b)

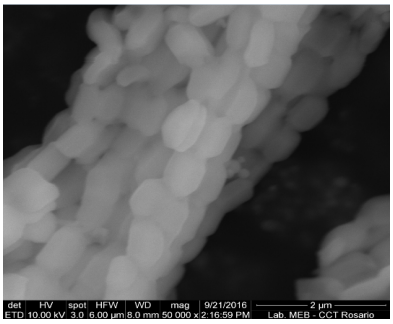

(c)

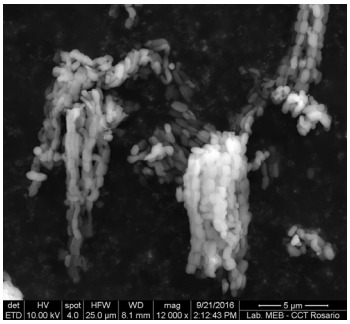

(d)

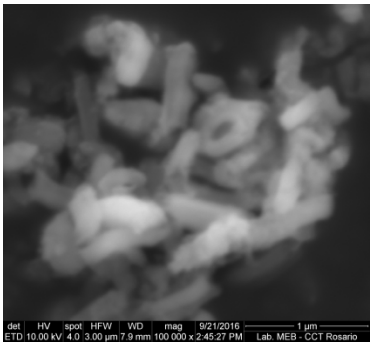

(e)

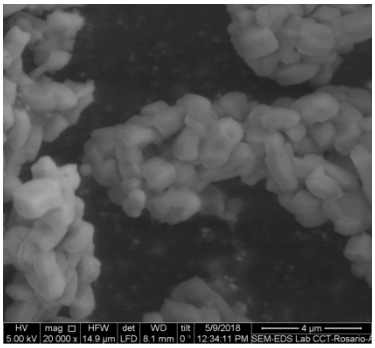

(f)

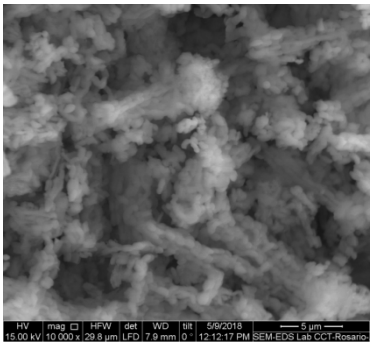

Figure 3

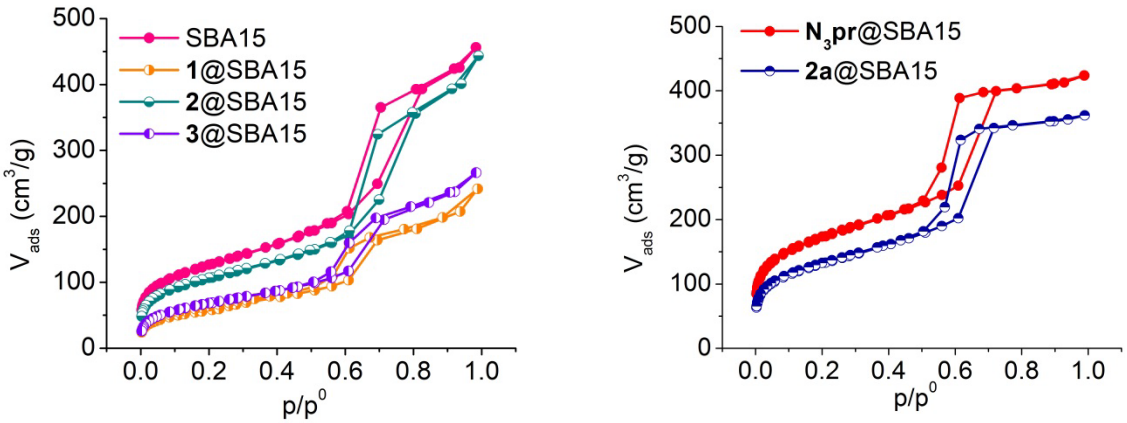
SBA15
1@SBA15
2@SBA15
3@SBA15
N3pr@SBA15
2a@SBA15
Vads (cm3/g)
p/p0
0
100
200
300
400
500
0.0
0.2
0.4
0.6
0.8
1.0

Figure 4

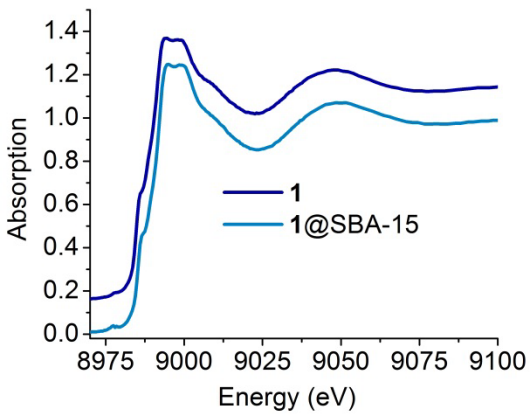
Absorption
Energy (eV)
1
1@SBA-15

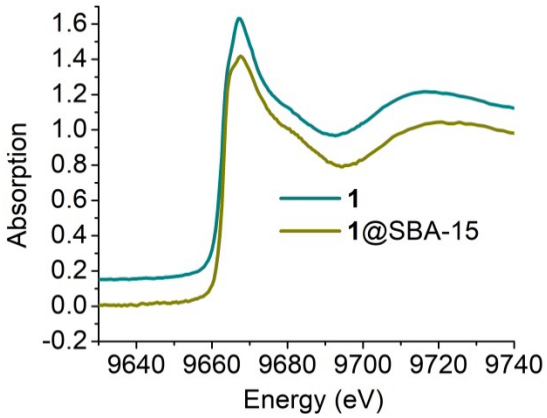
Absorption
Energy (eV)
1
1@SBA-15

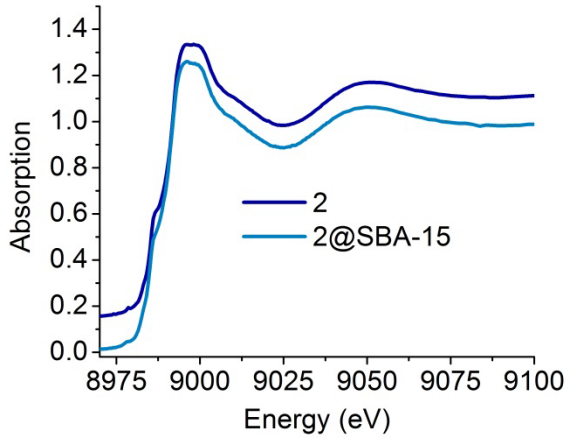
Absorption
Energy (eV)
2
2@SBA-15

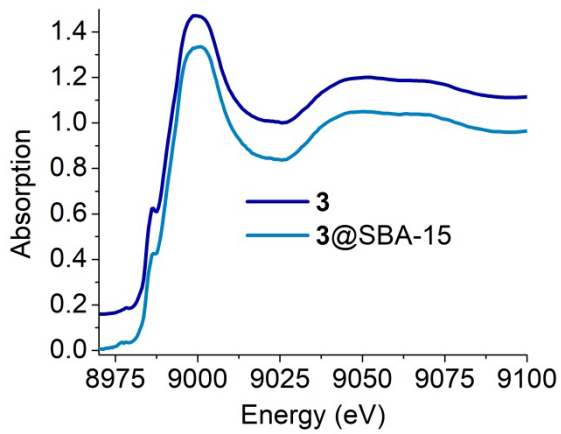
Absorption
Energy (eV)
3
3@SBA-15

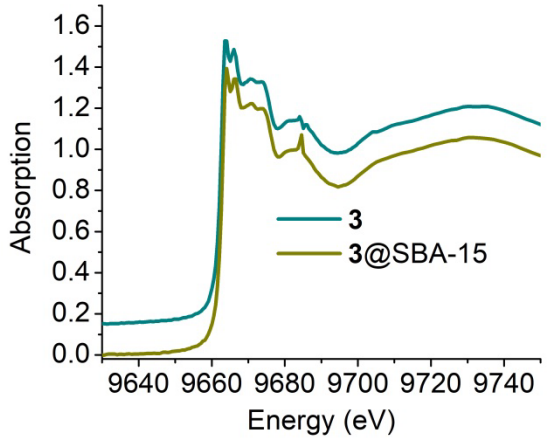
Absorption
Energy (eV)
3
3@SBA-15

Figure 5

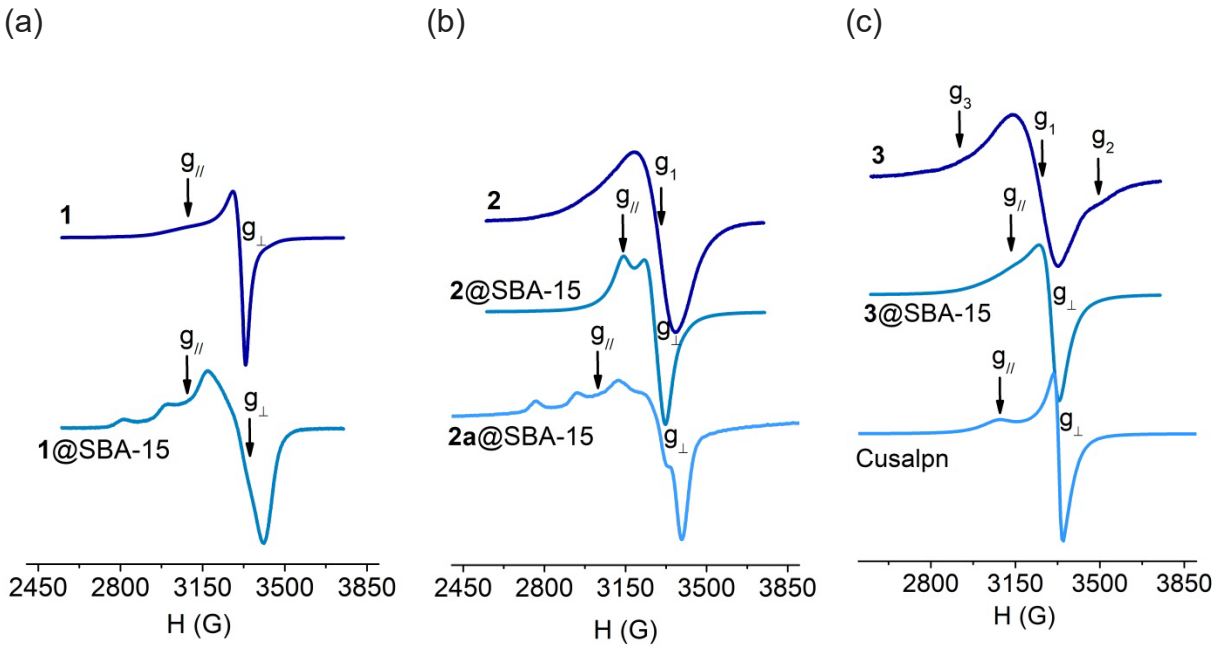
(a)
(b)
(c)
1
1@SBA-15
2
2@SBA-15
2a@SBA-15
3
3@SBA-15
Cusalpn
g//
g⊥
g1
g2
g3
2450 2800 3150 3500 3850
2800 3150 3500 3850
H (G)

Figure 6

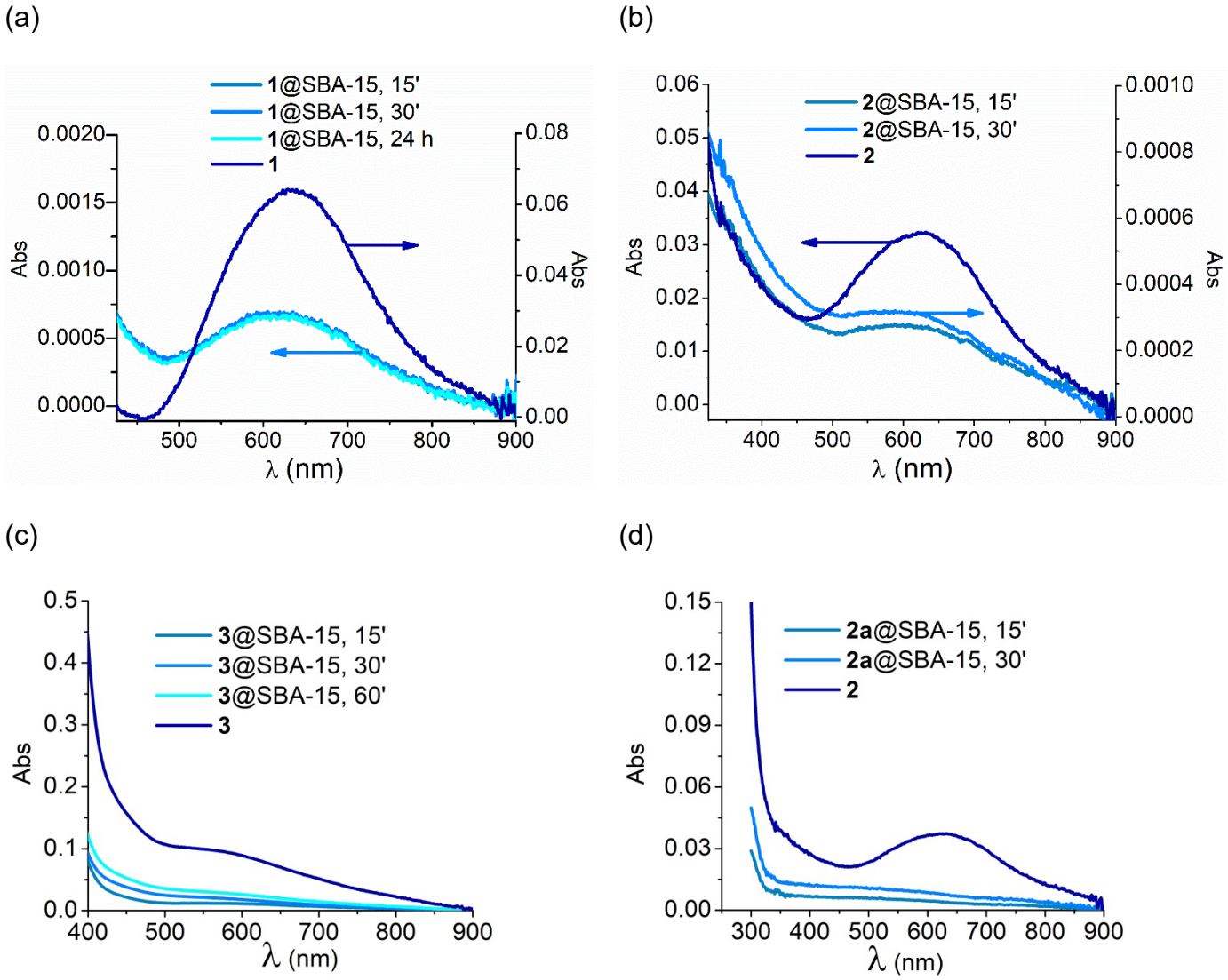
(a)
1@SBA-15, 15'
1@SBA-15, 30'
1@SBA-15, 24 h
1
Abs
λ (nm)
(b)
2@SBA-15, 15'
2@SBA-15, 30'
2
Abs
λ (nm)
(c)
3@SBA-15, 15'
3@SBA-15, 30'
3@SBA-15, 60'
3
Abs
λ (nm)
(d)
2a@SBA-15, 15'
2a@SBA-15, 30'
2
Abs
λ (nm)

Figure 7

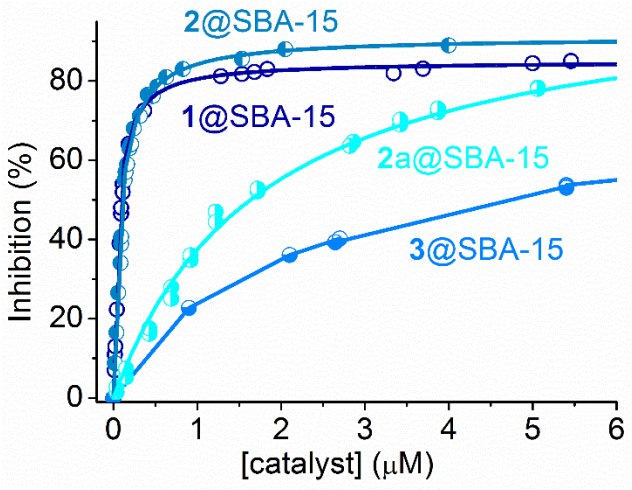
2@SBA-15
1@SBA-15
2a@SBA-15
3@SBA-15
Inhibition (%)
0
20
40
60
80
0
1
2
3
4
5
6
[catalyst] (μM)

Scheme 1

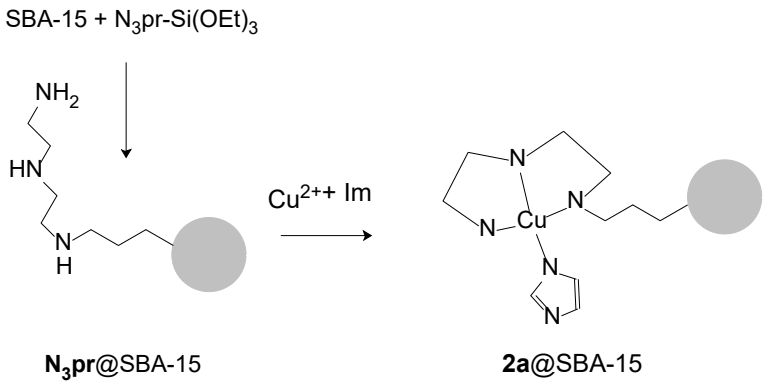

N_3pr@SBA-15 **2a**@SBA-15

Scheme 2

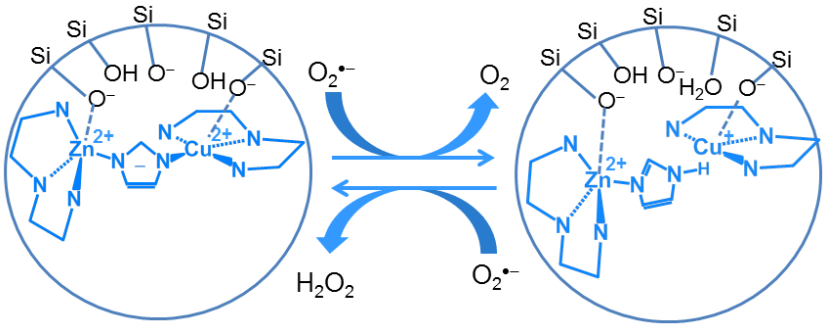
Si
Si
Si
Si
Si
OH
O⁻
OH
O⁻
O⁻
N
Zn
2+
N
N
N
N
Cu
2+
N
N
O₂•⁻
O₂
H₂O₂
O₂•⁻
Si
Si
Si
Si
Si
OH
O⁻
H₂O
O⁻
O⁻
N
Zn
2+
N
N–H
N
Cu
N
N
N
N